Proceedings of 2017 IEEE
International Conference on Mechatronics and Automation
August 6 - 9, Takamatsu, Japan

Design and Parameters Identification of Flexible Joint Robot

Wei Yin, Lei Sun, Meng Wang and Jingtai Liu
Institute of Robotics and Automatic Information System
NanKai University
Jinnan District, Tianjin, China
{*sunl, liujt*}*@nankai.edu.cn*

Xinwei Chen
Department of Computer Science
Minjiang University
Quanzhou, Fujian, China
109331123@qq.com

***Abstract*—This paper discusses design and parameters identification of a flexible joint robot (FJR) with 2 degrees of freedom. Design of a compact series elastic actuator (SEA) and hardware architecture of FJR, with each joint implemented an SEA, is introduced. To obtain relatively accurate parameters value in dynamic model of FJR, some identification methods of each term are detailed.**

***Index Terms*—Flexible joint robot, series elastic actuator, parameters identification**

I. INTRODUCTION

To acquire high position precision and wide bandwidth, typical actuation approach, like industrial robot, often makes use of rigid and non-backdrivable transmissions. On the contrary, compliant robots (CR) introduce elastic component in series with the energy source actively, which is a departure from traditional applications[1]. However, this behavior can offer a range of advantages over stiff actuators, like low output impedance, shock tolerance, energy storage, increased peak power output[2]. Moreover, elastic element between motor and load, on the one hand, can decrease the equivalent contact stiffness with environment, on the other hand, with elastic element, inertia of motor and transmission are decoupled from load, when collision happens, inertia associated with impact is reduced significantly. These properties offer a safer interaction among human, robots and environment. As a result, demands on CR have been rapidly increased to perform more dexterous and versatile tasks[3], [4].

As a member of CR, FJR has emerged as an important topic[5], including design and control. In general, each joint of FJR is driven by SEA[6], therefore, the key of FJR design is structure of SEA, and SEA design has received considerable attention. The first SEA was proposed by Ptatt in [7], and further studies was carried out in Robinson's Ph.D. research[8]. Since then, different structures of SEA were designed. In [9], Navvab etc. analysed the modeling and control of a compact arm equipped with semi-active friction dampers, and subsequently, they introduced a novel method that permitted the selection of joint stiffness of robotic arms powered by SEA[10]. In general, due to compromise on the selection of spring stiffness[11], SEA designs often have a problem of performance limitation, therefore, Emre etc. designed a novel SEA by using two spring in series[12], [13]: one is torsional hard and the other is linear soft. In [14], [15], an improved design of SEA was proposed, whose spring was installed in the chain of gears, so that small spring can be utilized, however, with small spring, capability of energy storage is reduced as well. Variable stiffness actuators extend the SEA concept by adding an additional motor to adjust the stiffness[16], [17], [18], [19], however, the design procedure is very difficult.

This paper discusses design and parameters identification of an FJR, detailed as the following 5 parts: Design of SEA and FJR is described in Section 2. Section 3 provides mathematical model of FJR. To identify each term in FJR dynamics, some identification methods are detailed in Section 4. Section 5 provides some summaries and future work.

II. FJR DESIGN

As main part of the FJR designed in this paper, SEA is shown in Fig. 1. Mechanical design of SEA is detailed in Fig. 1 (a), where 1 denotes geared motor, 3 represents link, 8 indicates absolute encoder, 6 denotes spring. Working process is illustrated in Fig. 1 (b), in equilibrium state, the two springs stay at A_1M and B_1N, respectively, when geared motor rotates a certain degrees, A_2M and B_2N become their new position, in this situation, torque generated by the two springs will drive link to move.

Fig. 2 shows details of FJR platform. The FJR is driven by Maxon DC servo motor with embedded coaxial encoders(4000PPR for first joint, 2000PPR for second joint) that can measure θ, while link position q is measured by Pepperl+Fuchs absolute encoder(65536PPR both), velocity signals are obtained by numerical differential operation. NI 9401 is utilized to read absolute encoders data and convey them to NI 9039, while NI 9881 works for communication between NI 9039 and motor drivers. NI 9039 is used to generate real-time control commands for FJR and receive control algorithm programmed in PC using LabVIEW.

This work is supported in part by National Natural Science Foundation (NNSF) under Grant 61573198, 15JCZDJC31200, MJUKF201733, STD Guide Project of Fujian under grant 2015H0031.

978-1-5090-6759-6/17/$31.00 ©2017 IEEE

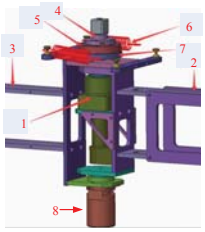

(a) SEA mechanical design

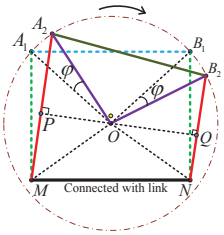

(b) Elasticity diagram

Fig. 1: SEA design

(a) Mechanical structure

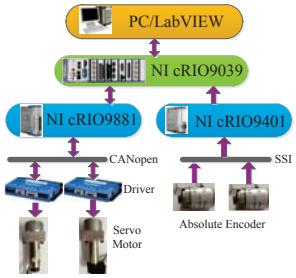

(b) Hardware architecture

Fig. 2: FJR Platform

III. MATHEMATICAL MODEL

Structure of platform designed in this paper satisfies the two assumptions made in [20], therefore, its dynamics is:

$$\begin{aligned} &M(q)\ddot{q} + C(q,\dot{q})\dot{q} + \tau_{fl}(q,\dot{q}) + G(q) = \tau_c(\varphi) \\ &J\ddot{\theta} + \tau_{fm}(\dot{\theta}) + \tau_c(\varphi) = \tau_m \\ &\tau_c(\varphi) = K\varphi = K(\theta - q) \end{aligned} \tag{1}$$

where representation of each term in (1) is explained as:

- $q \in \mathbb{R}^2$: position vector of link side
- $\theta \in \mathbb{R}^2$: position vector of motor side
- $M(q) \in \mathbb{R}^{2\times 2}$: inertia matrix of link side
- $C(q,\dot{q})\dot{q} \in \mathbb{R}^2$: coriolis and centripetal torque vector of link side
- $\tau_{fl}(q,\dot{q}) \in \mathbb{R}^2$: friction vector of link side
- $G(q) \in \mathbb{R}^2$: gravity vector of link side
- $\tau_c(\varphi) \in \mathbb{R}^2$: torque vector from elastic mechanism
- $K = \mathrm{diag}(K_1, K_2)$: stiffness matrix
- $J = \mathrm{diag}(J_1, J_2)$: inertia matrix of motor side
- $\tau_{fm}(\dot{\theta}) \in \mathbb{R}^2$: friction vector of motor side
- $\tau_m \in \mathbb{R}^2$: motor torque vector, e.g., control input

IV. PARAMETERS IDENTIFICATION

In this section, some methods are introduced for parameters identification of FJR.

A. Stiffness Identification

Stiffness identification process is described as follows. In this subsection, both first link and second link are fixed, i.e., $q_1 \equiv q_2 \equiv 0$, servo motor is configured in interpolated (IP) mode and rotates certain degrees and then back to initial position, and opposite direction experiences the same operation, detailed as follows.

$$\begin{aligned} \theta_1 &: \ 0 \to 0.3864 \to 0 \to -0.3864 \to 0(\mathrm{rad}) \\ \theta_2 &: \ 0 \to 0.2262 \to 0 \to -0.2262 \to 0(\mathrm{rad}) \end{aligned}$$

and step for θ_1 and θ_2 are both 4.7124×10^{-3}(rad). When motor moves one step within 100ms (instruction cycle of stiffness identification experiment), it stops for 9.9 seconds, that is, period of stiffness identification is 10 seconds, and data of the last two seconds is averaged as real value.

Identification results are shown in Fig. 3 and Fig. 4. It can be observed that there is hysteresis, especially in the first joint. The pink dots in each figure denote that motor moves from initial position to positive maximum value (PMV), the green dots represent motor rotates from PMV to initial position, while red dots indicate initial position to negative maximum value (NMV), and black dots show NMV to initial position.

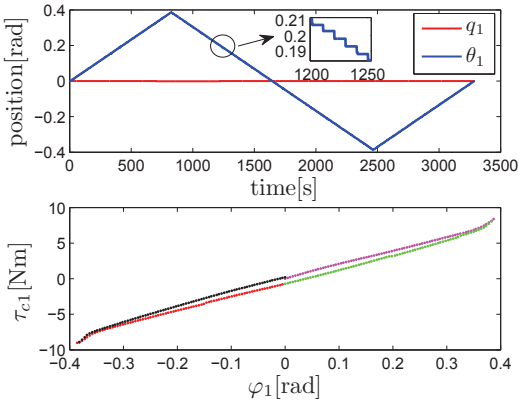

Fig. 3: Identification result of first joint stiffness

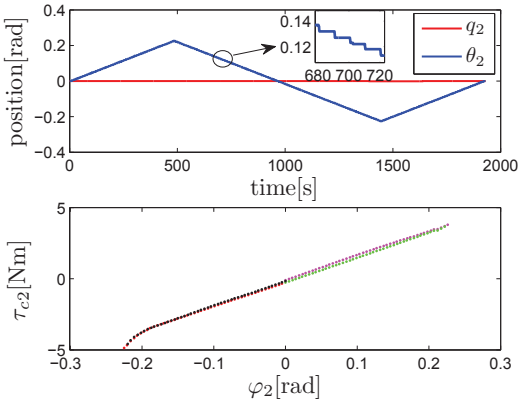

Fig. 4: Identification result of second joint stiffness

Via least square method (LSM), equivalent stiffness of SEA in each joint is identified as

$$K_1 = 20.48\text{Nm/rad},\ K_2 = 17.75\text{Nm/rad}$$

B. Gravity Identification

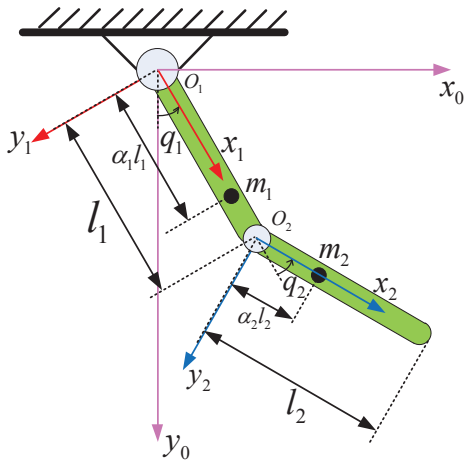

Fig. 5: Link side schematic diagram of FJR

Link side schematic diagram of FJR is shown in Fig. 5, where black spots denote CoM of each link, O_1 and O_2 represent each joint axis, respectively, and

- l_1, l_2 : length of first and second link, respectively;
- m_1, m_2 : mass of first and second link, respectively;
- $\alpha_1 l_1$: distance between O_1 and CoM of first link;
- $\alpha_2 l_2$: distance between O_2 and CoM of second link;

In coordinate system $O_1 x_0 y_0$, coordinate of CoM of each link can be obtained as follows

$$\vec{r}_1 = \alpha_1 \vec{l}_1\,;\ \ \vec{r}_2 = \vec{l}_1 + \alpha_2 \vec{l}_2 \tag{2}$$

On this basis, gravity term in dynamics (1) is detailed as

$$G_1 = \vec{r}_1 \times m_1 \vec{g} + \vec{r}_2 \times m_2 \vec{g};\ \ G_2 = \alpha_2 \vec{l}_2 \times m_2 \vec{g} \tag{3}$$

where $\vec{g}$ is gravitational acceleration. Combining (2) with (3) yields

$$\begin{aligned} G_1 &= (\alpha_1 m_1 g l_1 + m_2 g l_1)\sin(q_1) + \alpha_2 m_2 g l_2 \sin(q_1 + q_2) \\ G_2 &= \alpha_2 m_2 g l_2 \sin(q_1 + q_2) \end{aligned} \tag{4}$$

With second joint fixed, i.e., $\theta_2 \equiv q_2 \equiv 0$, the first equation of (4) can be rearranged as

$$G_1 = (\alpha_1 m_1 g l_1 + m_2 g l_1 + \alpha_2 m_2 g l_2)\sin(q_1) \tag{5}$$

leading to that G_1 is proportional to $\sin(q_1)$. Motor moves along the same trajectory as that in stiffness identification section expect the maximum value and step, that is

$$\theta_1 :\ 0 \to 1.2174 \to 0 \to -1.2174 \to 0(\text{rad})$$

and step for θ_1 is 7.8540×10^{-3} rad. Data operation is the same as that in stiffness identification process. Experiment result is shown in Fig. 6, slope of the second subfigure of Fig. 6 can be obtained via LSM, and the result is 6.70 Nm/rad, leading to that

$$\alpha_1 m_1 g l_1 + m_2 g l_1 + \alpha_2 m_2 g l_2 = 6.70 \tag{6}$$

With first joint fixed, i.e., $\theta_1 \equiv q_1 \equiv 0$, the second equation of (4) can be rearranged as $G_2 = \alpha_2 m_2 g l_2 \sin(q_2)$ which means that G_2 is proportional to $\sin(q_2)$. Motor trajectory for θ_2 is

$$\theta_2 :\ 0 \to 1.4608 \to 0 \to -1.4608 \to 0(\text{rad})$$

and step for θ_2 is 9.4248×10^{-3} rad. Data operation is also the same as that of stiffness identification process. Experiment result is shown in Fig. 7, slope of the second subfigure of Fig. 7 can be obtained via LSM, and the result is 0.53 Nm/rad, leading to that

$$\alpha_2 m_2 g l_2 = 0.53 \tag{7}$$

Combining (6) with (7) yields

$$G(q) = \begin{bmatrix} 6.17\sin(q_1) + 0.53\sin(q_1 + q_2) \\ 0.53\sin(q_1 + q_2) \end{bmatrix} \tag{8}$$

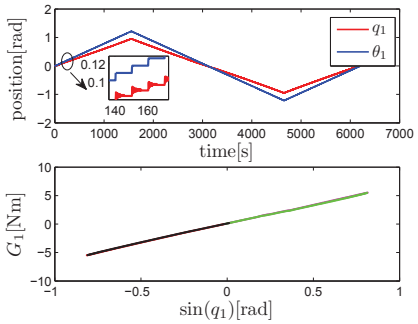

Fig. 6: Identification result of first joint gravity

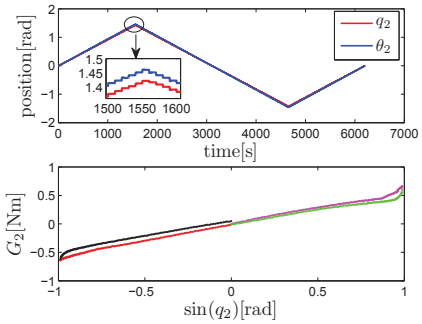

Fig. 7: Identification result of second joint gravity

C. Link Inertia Identification

In this subsection, FJR is placed parallel to the ground, therefore, gravity term can be ignored. With second joint fixed, i.e., $\theta_2 \equiv q_2 \equiv 0$, link side dynamics degenerates into the following form

$$\ddot{q}_1 + \frac{D_1}{I_1}\dot{q}_1 + \frac{K_1}{I_1}q_1 = \frac{K_1}{I_1}\theta_1 \tag{9}$$

which can be regarded as second order damped oscillation system. Where I_1 is Inertia of the whole link relative to joint axis 1, and D_1 is the damping ratio.

First motor is fixed to zero, that is, $\theta_1 \equiv 0$. In this situation, when an impulse is imposed on first link, it experiences damping oscillation, shown in the first subfigure of Fig. 8, and wave crest of q_1 (denoted by $q_{1\text{peak}}$) satisfies

$$q_{1\text{peak}}(t) = \frac{\omega_{s1}}{\sqrt{1-\zeta_1^2}}\exp(-\zeta_1\omega_{s1}t) \tag{10}$$

where

$$\omega_{s1} = \sqrt{\frac{K_1}{I_1}},\ \zeta_1 = \frac{D_1}{2\sqrt{K_1 I_1}} \tag{11}$$

After logarithm both sides of (10), it can be observed that $\ln q_{1\text{peak}}(t)$ is linear to time t, that is

$$\ln q_{1\text{peak}}(t) = -\zeta_1\omega_{s1}t + \ln\frac{\omega_{s1}}{\sqrt{1-\zeta_1^2}} \tag{12}$$

the slope $(-\zeta_1\omega_{s1})$ can be obtained via LSM, as shown in the second subfigure of Fig. 8, the result is -0.5745, that is,

$$-\zeta_1\omega_{s1} = -0.5745 \tag{13}$$

From Fig. 8, time interval between two adjacent wave crests is averaged as 0.6509 second, leading to

$$\frac{2\pi}{\omega_{s1}\sqrt{1-\zeta_1^2}} = 0.6509 \tag{14}$$

Invoking (13) and (14) into (11) and noting that $K_1 = 20.48\text{Nm/rad}$ results in

$$I_1 = 0.2190\text{kgm}^2$$

With first joint fixed, i.e., $\theta_1 \equiv q_1 \equiv 0$, and $\theta_2 \equiv 0$, an impulse is imposed on second link, the same treatment as above leads to result shown in Fig. 9. Inertia of second link relative to joint axis 2 is identified as

$$I_2 = 0.0116\text{kgm}^2$$

Based on definition of CoM, it can be obtained from Fig. 5 that

$$\alpha_1 l_1 = \frac{\sum_j m_{1j}x_{1j}}{m_1};\ \ \alpha_2 l_2 = \frac{\sum_j m_{2j}x_{2j}}{m_2} \tag{15}$$

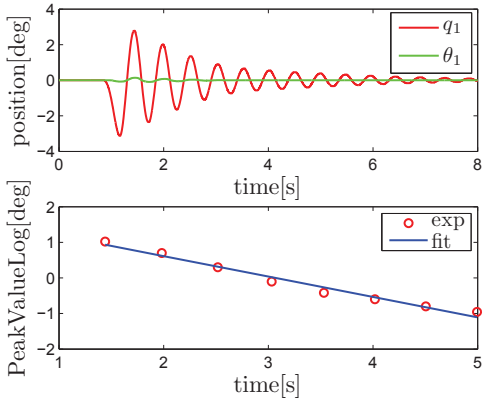

Fig. 8: Identification result of first joint frequency

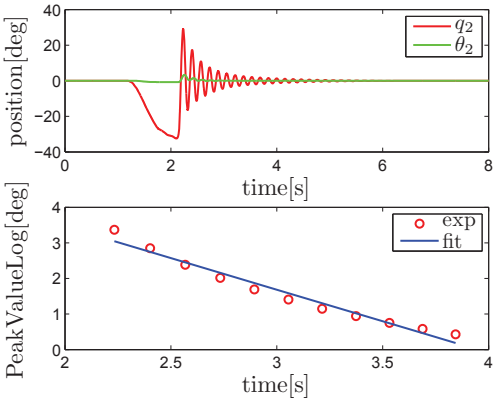

Fig. 9: Identification result of second joint frequency

And from definition of I_1 and I_2, we have

$$\begin{aligned} I_1 &= \sum_j m_{1j}x_{1j}^2 + \sum_j m_{2j}(l_1 + x_{2j})^2 \\ I_2 &= \sum_j m_{2j}x_{2j}^2 \end{aligned} \tag{16}$$

Let M_1 be inertia of first link relative to joint axis 1, and M_2 be inertia of second link relative to its CoM, respectively, considering parallel axis theorem, M_1 and M_2 are in the following form

$$M_1 = \sum_j m_{1j}x_{1j}^2;\ \ M_2 = \sum_j m_{2j}x_{2j}^2 - m_2(\alpha_2 l_2)^2 \tag{17}$$

Combining (15), (16) and (17) yields

$$\begin{aligned} M_1 &= I_1 - m_2 l_1^2 - I_2 - 2\alpha_2 m_2 l_1 l_2 \\ M_2 &= I_2 - m_2(\alpha_2 l_2)^2 \end{aligned} \tag{18}$$

System parameters of FJR designed in this paper are

$$\begin{aligned} l_1 &= 0.345\text{ m},\ m_1 = 1.570\text{ kg} \\ l_2 &= 0.305\text{ m},\ m_2 = 0.660\text{ kg} \end{aligned}$$

Invoking system parameters into (6) and (7) yields

$$\alpha_1 = 0.7420,\ \alpha_2 = 0.2687$$

thus

$$M_1 = 0.0915\text{kgm}^2,\ M_2 = 7.1672 \times 10^{-3}\text{kgm}^2$$

D. Link Side Dynamics

Based on analysis above, kinetic energy of link side is

$$K_{in} = \frac{1}{2}M_1\dot{q}_1^2 + \frac{1}{2}M_2(\dot{q}_1 + \dot{q}_2)^2 + \frac{1}{2}m_2v_2^2 \tag{19}$$

where v_2 is velocity of CoM of second link in coordinate system $O_1x_0y_0$, and

$$\begin{aligned} v_2^2 = {} & [l_1^2 + \alpha_2^2 l_2^2 + 2\alpha_2 l_1 l_2 \cos(q_2)]\dot{q}_1^2 + \alpha_2^2 l_2^2 \dot{q}_2^2 \\ & + [2\alpha_2^2 l_2^2 + 2\alpha_2 l_1 l_2 \cos(q_2)]\dot{q}_1\dot{q}_2 \end{aligned} \tag{20}$$

Potential energy of link side is

$$\begin{aligned} P_{ot} = {} & (\alpha_1 m_1 g l_1 + m_2 g l_1)[1 - \cos(q_1)] \\ & + \alpha_2 m_2 g l_2 [1 - \cos(q_1 + q_2)] \end{aligned} \tag{21}$$

Based on Lagrange dynamic equation, each term of link side in (1) can be calculated as follows.

$$M(q) = \begin{bmatrix} M_{11} & M_{12} \\ M_{21} & M_{22} \end{bmatrix};\ C(q,\dot{q}) = \begin{bmatrix} C_{11} & C_{12} \\ C_{21} & C_{22} \end{bmatrix} \tag{22}$$

where

$$\begin{aligned} M_{11} &= M_1 + M_2 + m_2[l_1^2 + \alpha_2^2 l_2^2 + 2\alpha_2 l_1 l_2 \cos(q_2)] \\ M_{12} &= M_{21} = M_2 + m_2\alpha_2^2 l_2^2 + \alpha_2 m_2 l_1 l_2 \cos(q_2) \\ M_{22} &= M_2 + m_2\alpha_2^2 l_2^2 \\ C_{11} &= -2\alpha_2 m_2 l_1 l_2 \dot{q}_2 \sin(q_2) \\ C_{12} &= -\alpha_2 m_2 l_1 l_2 \dot{q}_2 \sin(q_2) \\ C_{21} &= \alpha_2 m_2 l_1 l_2 \dot{q}_1 \sin(q_2);\ \ C_{22} = 0 \end{aligned} \tag{23}$$

With all parameters identified before, $M(q)$ and $C(q,\dot{q})$ can be obtained via (23).

Since friction of link side, i.e., $\tau_{fl}(q,\dot{q})$ is damping term in controller design, it is not necessary to model it.

E. Motor Friction Identification

In this subsection, servo motor is configured in velocity mode without payload, i.e., link is removed. Motor rotates with a constant speed v, and torque obtained from amplifier is regarded as friction corresponding to the very speed, when v changes its value, friction under different velocities can be identified. Experiment results are shown in Fig. 10, where red hollow dots represent experiment data. Therefore, motor friction is modeled as

$$\begin{aligned} & \tau_{fmi}(\dot{\theta}_i) = B_i\dot{\theta}_i + \tau_{fmi-nonlinear}(\dot{\theta}_i) \\ & \tau_{fmi-nonlinear}(\dot{\theta}_i) \\ & = f_i \tanh\left(\frac{\dot{\theta}_i}{\eta_i}\right) - f_i\omega_i \tanh\left[\frac{\dot{\theta}_i}{\eta_i} - h_i \tanh\left(\frac{\dot{\theta}_i}{\eta_i}\right)\right] \end{aligned} \tag{24}$$

where $i = 1, 2$, via nonlinear LSM, parameters in (24) are identified as follows.

$$\begin{aligned} & f_1 = 1.123, \quad \eta_1 = 0.9505 \\ & \omega_1 = -0.7154, \quad h_1 = -6539.2, \quad B_1 = 0.4968 \\ & f_2 = 0.8607, \quad \eta_2 = 0.0174 \\ & \omega_2 = -0.1019, \quad h_2 = 11.9636, \quad B_2 = 0.5051 \end{aligned}$$

The fit curve of motor friction is shown in Fig. 10 with green line.

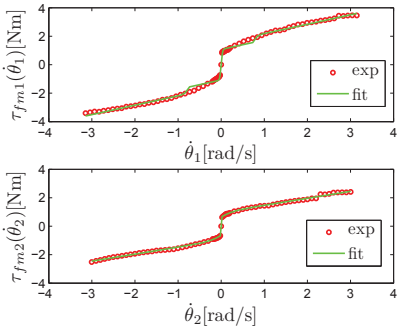

Fig. 10: Identification result of motor friction

F. Motor Inertia Identification

In this subsection, servo motor is configured in torque mode without payload, i.e., link is removed. Thus, motor dynamics is

$$\tau_{mi} = J_i\ddot{\theta}_i + B_i\dot{\theta}_i + \tau_{fmi-nonlinear}(\dot{\theta}_i) \tag{25}$$

and control input τ_{mi} is designed as

$$\tau_{mi} = u_i + \tau_{fmi-nonlinear}(\dot{\theta}_i) \tag{26}$$

Combining (25) with (26) yields

$$u_i = J_i\ddot{\theta}_i + B_i\dot{\theta}_i \tag{27}$$

thus, velocity response can be regarded as a first order inertia element. Motor rotates with a constant torque u_i, and velocity obtained from amplifier is regarded as response corresponding to the very torque, when u_i changes its value, velocity response under different torques can be obtained.

Experiment results of first joint motor are shown in Fig. 11 and Fig. 12, where curves with different color represent different u_i. Time constant $\frac{J_i}{B_i}$ of (27) can be obtained through the slope of each curve at initial moment in average, and result is $J_1 = 0.0686\ \text{kgm}^2$.

Inertia identification process of second joint motor is familiar to that of first joint motor, and is omitted here, identification results are shown in Fig. 13 and 14, and motor inertia is $J_2 = 0.0145\ \text{kgm}^2$.

So far, all parameters in FJR dynamics are identified except $\tau_{fl}(q,\dot{q})$.

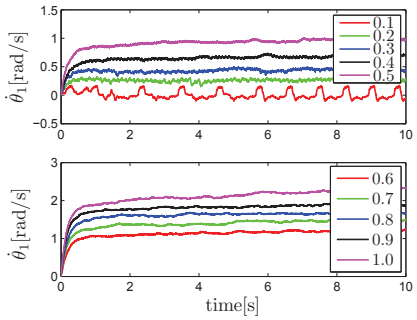

Fig. 11: Velocity response of 1st motor under different u_1

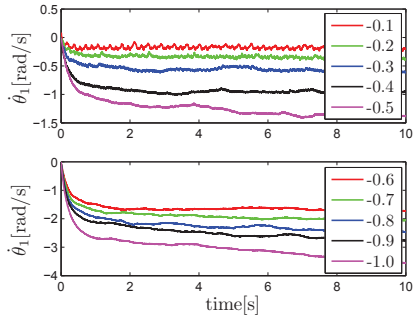

Fig. 12: Velocity response of 1st motor under different u_1

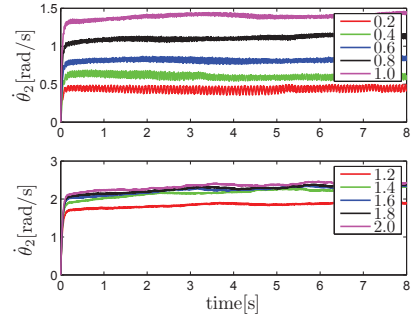

Fig. 13: Velocity response of 2nd motor under different u_2

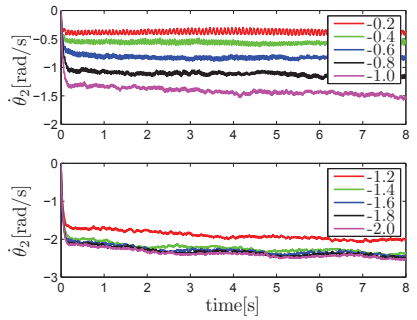

Fig. 14: Velocity response of 2nd motor under different u_2

V. CONCLUSION & FUTURE WORK

In summary, an FJR powered by SEA is designed and parameters in dynamics is identified in this paper. Control issues of FJR are under research.

REFERENCES

[1] Paine N, Oh S, Sentis L. Design and Control Considerations for High-Performance Series Elastic Actuators[J]. IEEE/ASME Transactions on Mechatronics, 2014, 19(3):1080-1091.

[2] Li X, Pan Y, Chen G, et al. Adaptive HumanCRobot Interaction Control for Robots Driven by Series Elastic Actuators[J]. IEEE Transactions on Robotics, 2017, 33:1-14.

[3] Tadele T S, Vries T D, Stramigioli S. The Safety of Domestic Robotics: A Survey of Various Safety-Related Publications[J]. IEEE Robotics & Automation Magazine, 2014, 21(3):134-142.

[4] Fujimoto Y, Murakami T, Oboe R. Advanced Motion Control for Next-Generation Industrial Applications[J]. IEEE Transactions on Industrial Electronics, 2016, 63(3):1886-1888.

[5] Min J K, Wan K C. Disturbance-Observer-Based PD Control of Flexible Joint Robots for Asymptotic Convergence[J]. IEEE Transactions on Robotics, 2015, 31(6):1-9.

[6] Petit F, Dietrich A, Albu-Schaffer A. Generalizing Torque Control Concepts: Using Well-Established Torque Control Methods on Variable Stiffness Robots[J]. IEEE Robotics & Automation Magazine, 2015, 22(4):37-51.

[7] Pratt G A, Williamson M M. Series elastic actuators[C]//Intelligent Robots and Systems, 1995 IEEE/RSJ International Conference on. IEEE, 1995, 1: 399-406.

[8] Robinson D W. Design and analysis of series elasticity in closed-loop actuator force control[J]. 2000.

[9] Kilpatrick K, Lavoie-Tremblay M, Ritchie J A, et al. Dynamic modeling and adaptable control of the $\mathrm{CompAct}^{\mathrm{TM}}$ arm[C]// IEEE International Conference on Mechatronics. IEEE, 2013:477-482.

[10] Kashiri N, Tsagarakis N G, Laffranchi M, et al. On the stiffness design of intrinsic compliant manipulators[C]// Ieee/asme International Conference on Advanced Intelligent Mechatronics. IEEE, 2013:1306-1311.

[11] Yu H, Huang S, Chen G, et al. Control design of a novel compliant actuator for rehabilitation robots[J]. Mechatronics, 2013, 23(8):1072C1083.

[12] Sariyildiz E, Chen G, Yu H. Robust position control of a novel series elastic actuator via disturbance observer[C]// Ieee/rsj International Conference on Intelligent Robots and Systems. IEEE, 2015:5423-5428.

[13] Sariyildiz E, Chen G, Yu H. An Acceleration-Based Robust Motion Controller Design for a Novel Series Elastic Actuator[J]. IEEE Transactions on Industrial Electronics, 2016, 63(3):1900-1910.

[14] Kong K, Bae J, Tomizuka M. A compact rotary series elastic actuator for knee joint assistive system[C]// IEEE International Conference on Robotics and Automation, ICRA 2010, Anchorage, Alaska, Usa, 3-7 May. DBLP, 2010:2940-2945.

[15] Kong K, Bae J, Tomizuka M. A Compact Rotary Series Elastic Actuator for Human Assistive Systems[J]. IEEE/ASME Transactions on Mechatronics, 2012, 17(2):288-297.

[16] Wolf S, Hirzinger G. A new variable stiffness design: Matching requirements of the next robot generation[C]// International Conference on Robotics and Automation. DLR, 2008:1741-1746.

[17] Albu-Schaffer A, Wolf S, Eiberger O, et al. Dynamic modelling and control of variable stiffness actuators[C]// IEEE International Conference on Robotics and Automation. IEEE, 2010:2155-2162.

[18] Wolf S, Eiberger O, Hirzinger G. The DLR FSJ: Energy based design of a variable stiffness joint[C]// IEEE International Conference on Robotics and Automation. IEEE, 2011:5082-5089.

[19] Grebenstein M, Albu-Schaffer A, Bahls T, et al. The DLR hand arm system[C]// IEEE International Conference on Robotics and Automation. DBLP, 2011:3175-3182.

[20] Spong M W. Modeling and Control of Elastic Joint Robots[J]. Asme Journal of Dyn.sys.meas. & Cont, 1987, 109(4):310-319.